

Space Weather



RESEARCH ARTICLE

10.1029/2019SW002355

Key Points:

- High-resolution model of exospheric temperatures developed
- When used with the NRLMSISE-00 code, better predictions of neutral density can be obtained
- During large geomagnetic storms, substantial increases in the exospheric temperatures occur in the polar regions

Correspondence to:

D. Weimer,
dweimer@vt.edu

Citation:

Weimer, D. R., Mehta, P. M., Tobiska, W. K., Doornbos, E., Mlynczak, M. G., Drob, D. P., & Emmert, J. T. (2020). Improving neutral density predictions using exospheric temperatures calculated on a geodesic, polyhedral grid. *Space Weather*, 18, e2019SW002355. <https://doi.org/10.1029/2019SW002355>

Received 16 SEP 2019

Accepted 7 DEC 2019

Accepted article online 10 DEC 2019

Improving Neutral Density Predictions Using Exospheric Temperatures Calculated on a Geodesic, Polyhedral Grid

D. R. Weimer^{1,2}, P. M. Mehta³, W. K. Tobiska⁴, E. Doornbos⁵, M. G. Mlynczak⁶, D. P. Drob⁷, and J. T. Emmert⁷

¹Center for Space Science and Engineering Research, Virginia Tech, Blacksburg, VA, USA, ²National Institute of Aerospace, Hampton, VA, USA, ³Department of Mechanical and Aerospace Engineering, Statler College of Engineering and Mineral Resources, West Virginia University, Morgantown, WV, USA, ⁴Space Environment Technologies, Los Angeles, CA, USA, ⁵Royal Netherlands Meteorological Institute (KNMI), De Bilt, The Netherlands, ⁶Science Directorate, NASA Langley Research Center, Hampton, VA, USA, ⁷Space Science Division, U.S. Naval Research Laboratory, Washington, DC, USA

Abstract A new model of exospheric temperatures has been developed, with the objective of predicting global values with greater spatial and temporal accuracy. From these temperatures, the neutral densities in the thermosphere can be calculated, through use of the Naval Research Laboratory Mass Spectrometer and Incoherent Scatter radar Extended (NRLMSISE-00) model. The exospheric temperature model is derived from measurements of the neutral densities on several satellites. These data were sorted into triangular cells on a geodesic grid, based on location. Prediction equations are derived for each grid cell using least error fits. Several versions of the model equations have been tested, using parameters such as the date, time, solar radiation, and nitric oxide emissions, as measured with the Sounding of the Atmosphere using Broadband Emission Radiometry (SABER) instrument on the Thermosphere Ionosphere Mesosphere Energetics and Dynamics (TIMED) satellite. Accuracy is improved with the addition of the total Poynting flux flowing into the polar regions, from an empirical model that uses the solar wind velocity and interplanetary magnetic field. Given such inputs, the model can produce global maps of the exospheric temperature. These maps show variations in the polar regions that are strongly modulated by the time of day, due to the daily rotation of the magnetic poles. For convenience the new model is referred to with the acronym EXEMPLAR (EXospheric TEMperatures on a PoLyhedral gRid). Neutral densities computed from the EXEMPLAR-NRLMSISE-00 models combined are found to produce very good results when compared with measured values.

Plain Language Summary Variations in the density of the upper atmosphere have long been a problem for accurate determination of the drag on satellites and their orbital paths. Long- and short-term fluctuations in solar radiation are one factor that influences this density; the energy dissipated by auroral electric fields and currents in the polar ionospheres also results in significant changes in the density of the neutral atoms at high altitudes, in the region known as the thermosphere. Some numerical models that calculate the density in the thermosphere rely on a prediction of the temperature at the top of the thermosphere, known as the exospheric temperature. A new method for forecasting these temperatures has been developed, based on satellite-based measurements of the atmospheric density. Exospheric temperatures that were derived from these measurements were divided up into triangular grid cells that uniformly cover a sphere. The collected temperatures in each grid cell, along with their associated dates, times, and other measurements, were used to develop a predictive formula, which is unique to each cell. When combined together, global maps of the temperatures are obtained. This method is named using the acronym EXEMPLAR, EXospheric TEMperatures on a PoLyhedral gRid.

1. Introduction

Variations in the density of the upper atmosphere have long been a problem for accurate determination of the drag on satellites and their orbital paths. Long- and short-term fluctuations in solar radiation are one factor that influences this density; the energy dissipated by auroral electric fields and currents in the

©2019. The Authors.

This is an open access article under the terms of the Creative Commons Attribution-NonCommercial-NoDerivs License, which permits use and distribution in any medium, provided the original work is properly cited, the use is non-commercial and no modifications or adaptations are made.

polar ionospheres also results in significant changes in the density of the neutral atoms and molecules. Due to the increasing temperatures above altitudes of 80–90 km, this region is known as the thermosphere. Above altitudes of 200 km the temperature asymptotically approaches a limiting value, the thermopause temperature, also known as the exospheric temperature (Prölss & Bird, 2004), often abbreviated as either T_{ex} or T_{∞} .

A number of methods have been developed in order to help improve the predictions of the neutral density, including both empirical models and numerical simulations. For a brief description of some models and methods used to assess performance, refer to Shim et al. (2012) and Bruinsma et al. (2018).

It had been found by Weimer et al. (2015) that nitric oxide (*NO*) emissions from the thermosphere had strong correlation with auroral energy dissipation and higher cooling rates following geomagnetic storms. It was also found that the *NO* emissions were positively correlated with the exospheric temperatures, including the solar EUV component, later verified with global maps of statistical averages (Weimer et al., 2016). The measurements of these infrared emissions from *NO* were obtained with the Sounding of the Atmosphere using Broadband Emission Radiometry (SABER) instrument on the Thermosphere Ionosphere Mesosphere Energetics and Dynamics (TIMED) spacecraft (Mlynczak et al., 2005, 2010). The initial objective of this project was to determine whether or not such measurements of nitric oxide emissions in the thermosphere could be used to improve forecasts of exospheric temperatures. The best way to accomplish this objective was to experiment with empirical models of the exospheric temperatures, using the *NO* emissions in some versions, to determine whether or not improved predictions could be obtained. The end result was an empirical model that can more accurately predict the exospheric temperatures. Through the use of the MSIS model, better predictions of the neutral density are also obtained. The purpose of this paper is to provide a detailed scientific rationale for the basis functions chosen for the new model (presently under development) and highlight the significance of initial results through data-model comparisons.

The various versions of this empirical model are derived from temperature measurements that are sorted according to their location on a geodesic grid. A multiple linear regression fit is used with the data in each grid cell to derive an expression for the temperature at that cell's specific location, as a function of the input parameters. The choice of the specific input parameters that are included in the model formulas are varied in order to determine which combinations can produce the most accurate results.

2. Derivation of Exospheric Temperatures

The exospheric temperatures that are used here are derived from neutral density measurements, employing much the same methodology as described by Weimer et al. (2016). The thermosphere density model, known as the Naval Research Laboratory Mass Spectrometer and Incoherent Scatter radar Extended (NRLMSISE-00) model (Hedin, 1991; Picone et al., 2002), is employed. Abbreviated herein as simply “MSIS,” this model provides as a function of altitude and geographical location the density of several atomic and molecular species, as well as temperature. The input parameters for MSIS are the date, time, the solar $F_{10.7}$ index, and geomagnetic activity. This activity is provided as the daily A_p index, and six additional, 3-hr ap indices as an option. Control flags input to MSIS can turn on or off various parts of the model's calculations.

The MSIS model can calculate the expected density value from a given geographic location, including altitude, along with the other expected input parameters. Internally, MSIS calculates the exospheric temperature for the given coordinates; this exospheric temperature is used to compute the density of each species as a function of altitude, starting at the 120-km altitude boundary where the neutral composition and other conditions are specified by MSIS. In this work the MSIS model is used backward in order to derive the exospheric temperatures from the density values that are measured on various satellites. If the predicted value of the total density does not match the measured value, then exospheric temperature is varied (through a modification of the code) until the measured and predicted densities match. Specifically, the bisection method (also known as the interval halving or binary search method) is used until the temperature is resolved to within 2° K.

The neutral density data that we use have been acquired on four different satellites. One set of data are from the Challenging Mini-satellite Payload (CHAMP) satellite [Bruinsma et al., 2004], having measurements in the years 2002 to 2009. The second data set is from the Gravity Recovery and Climate Experiment (GRACE) satellites (Tapley et al., 2004), from 2003 to 2010. Of the two GRACE satellites, only data from

the “A” satellite are used, as these two satellites are in nearly identical orbits. The density values had been recalculated by Mehta et al. (2017) and are available with temporal cadence of 10 s for CHAMP and 5 s for GRACE A, which is at a higher altitude. Both the CHAMP and GRACE neutral densities are derived from accelerometer measurements of the orbital drag forces.

The other two data sets are from the European Space Agency's Swarm mission, consisting of three identical satellites (Swarm A, B, and C) (Friis-Christensen et al., 2006) that were launched on 22 November 2013. The Swarm A and C spacecraft orbit at an altitude of approximately 470 km, and Swarm B orbits at about 520-km altitude. Since the A and C spacecraft are so close together and provide essentially the same drag values at the same times and similar locations, only the Swarm A and B data are used. The Swarm data that are included in this study start on 30 November 2013 and include all of years 2014 to 2017 for Swarm A and through June 2016 for Swarm B. These density data are obtained from precise orbit determinations using the Global Positioning System (GPS) receivers on the spacecraft (Astafyeva et al., 2017).

As this study required uniform, global coverage at all local times, neutral density measurements from the European Space Agency's Gravity field and Ocean Circulation Explorer (GOCE) mission (Doornbos et al., 2014) were not used, as this satellite orbited at a near fixed local time. Additionally, the GOCE satellite was at a very low altitude, under 300-km altitude, where variations in the exospheric temperature resulted in relatively small changes in the neutral density. Due to this low dynamic range, oftentimes the exospheric temperatures derived from the GOCE neutral density measurements would seem to be unreasonably high or low.

Corrections were made to the original density values, following the procedure that is described in detail by Weimer et al. (2018). Briefly, the neutral densities obtained from each satellite were compared with global values obtained by Emmert (2009), from an analysis of the orbits of approximately 5,000 objects. As a result of this comparison, it was found that multiplying the CHAMP densities by 1.12, the Swarm A densities by 1.08, and the Swarm B densities by 1.08 brought the various data sets into agreement. The corrections applied to the density values from GRACE A varied with time, starting with a multiplication factor of 1.25 prior to 2004, 1.33 in 2004 and 2005, and 1.24 in 2006 and later. The cause of this change was a reversal of the positions of the GRACE A and B satellites in December 2005, so that the trailing satellite became the leading satellite, and at the same time, the fore and aft ends were reversed in order to keep their radar antennas pointing at each other. This switch had changed their coefficient of drag and the resulting densities (Weimer et al., 2018).

As the existing MSIS model was developed prior to the unusually low solar minimum in 2008–2009, it does not represent very well the anomalously low densities that were observed. Therefore, some adjustments were applied within MSIS to compensate, originating from the methodology of Emmert (2009). Perturbations to the density values at the 120-km altitude boundary in MSIS were applied as a function of time. One factor, expressed as a percentage, was applied to everything except the atomic oxygen, while another adjustment applied to only the oxygen. These data originated from Emmert et al. (2010) and Emmert et al. (2014). Percentages that were provided as daily values were smoothed using a 27-day running average; being one solar rotation, this averaging smooths out the effects of active sunspot regions. Although these data end before 2014, the percentages were extended to cover the Swarm time period through fitting the correction factors with the global NO and carbon dioxide emissions that were measured with SABER, as demonstrated by Weimer et al. [2018].

3. The Geodesic Polyhedral Grid

As mentioned earlier, the empirical model (and variations) are derived from temperature measurements that are sorted according to their location on a geodesic grid. Statistical averages resulting from a similar, spatial binning of temperature measurements were previously shown by Weimer et al. (2016), in which equal-area, quadrilateral pixels (Górski et al., 2005) were used. While that particular gridding scheme divided a sphere into exactly equal areas, the grid resolutions that are available were determined to be either too small or large for this project, with the Górski et al. (2005) grid limited to only 12, 48, 192, 768, 3,072, 12,288, 491,452, or greater number of elements. Subsequently, a switch was made to a different type of spherical grid that had the desired flexibility in the number of grid cells.

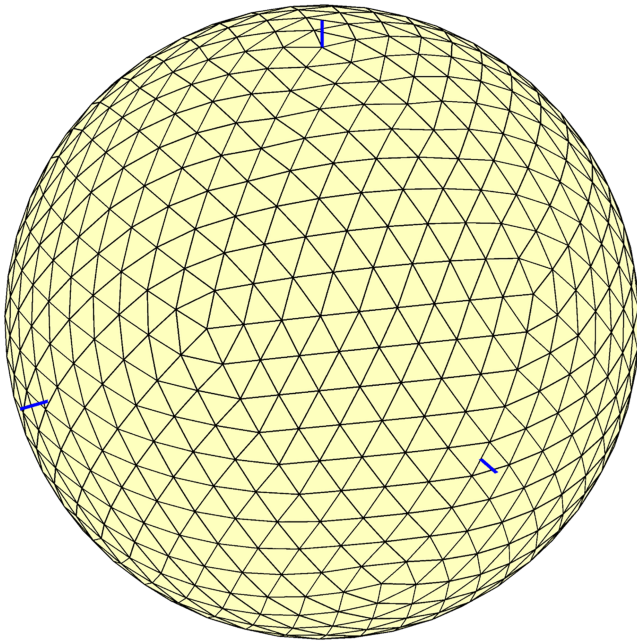


Figure 1. Illustration of the geodesic, polyhedral grid. The grid that is used for this project is derived from a 20-face icosahedron, which has each face subdivided into 81 equilateral triangles, resulting in 1,620 triangles, that are projected to a spherical surface. For reference, the blue lines show three orthogonal axes, with one pole at the top.

The final grid that is used is based on an icosahedron, a polyhedron having 20 faces that are equilateral triangles (Wenninger, 2014). Each face is then divided into m divisions on each edge, or $T = m^2$ triangles, with the new vertices then projected outward to a sphere. For our purpose $m = 9$ and $T = 81$ was chosen, resulting in 1,620 faces (https://en.wikipedia.org/wiki/List_of_geodesic_polyhedra_and_Goldberg_polyhedra#Icosahedral). This grid is illustrated in Figure 1. The edges of the triangles span approximately 7° , while the centers of the adjacent triangles range from approximately 4.3° to 9.9° . While the areas of the faces are not exactly equal, the areas are all within 10.6% of the mean. While a greater number of faces provides a higher spatial resolution, it also reduces the density of samples in each cell, which can produce greater statistical noise in the results.

Each exospheric temperature data point is assigned to a cell based on the geographic coordinates where the measurement was taken. The local solar time of each datum, converted into degrees, is used for longitude, with local noon placed at 0° longitude. Following this sorting, the number of points in each pixel/cell ranges from 28,477 to 542,195, with the largest numbers found around the poles due to the high inclinations of all satellite orbits.

4. Model Formulation

Following the sorting of data into grid cells according to their location, the next step was fitting these data to obtain an expression (to be described) for the exospheric temperature in each cell, using a multiple linear regression

(least error fit). Therefore, 1,620 separate fits are done. Various independent variables were tried, as well as different combinations of variables. These trials were eventually reduced to seven basic versions of the temperature equations for comparison.

After the multiple linear regression fits are done, the 1,620 sets of coefficients could be used as is. Without any further processing, the satellite orbits that occurred during particularly active or inactive times tended to produce uneven results. Increasing the resolution of the grid makes this problem even worse. In order to reduce such artifacts, each coefficient was smoothed by taking the mean value of the same coefficient in neighboring grid cells (using all triangles that contain a common vertex). Afterward, all temperature values are compared with the fitted values in order to compute the standard deviation and mean absolute deviation, separately for each grid cell, then using the mean values of the standard and absolute deviations of all cells, in order to assess model performance.

In order to provide this new empirical model with a name that distinguishes it from others, the acronym EXEMPLAR is given, from EXospheric TEMperatures on a PoLyhedrAl gRid. The misspelling of “exemplar” is deliberate in order to avoid confusion with acronyms already in use.

4.1. Version 0: Solar Indices Only

The most basic version of the new model relies on solar indices only, as a reference point for later improvements. While the standard $F_{10.7}$ solar index is well known, Tobiska et al. (2008) and Bowman et al. (2008) had defined additional solar indices that function in a similar manner. These indices are used in the Jacchia-Bowman density model (JB2008). As indicated by Bowman et al. (2008), “the solar index F_{10} is really a proxy index because it is measured at a 10.7-cm wavelength, which is not a direct measure of any ultraviolet radiation and is not absorbed by the atmosphere.” Additional indices used in the JB2008 model are S_{10} , M_{10} , and Y_{10} , which are based on wavelengths that are absorbed. They are named to suggest their relationship to the F_{10} index (a shortened notation), to which they are calibrated. Briefly, the S_{10} index is derived from EUV flux measured with the the Solar Extreme-ultraviolet Monitor (SEM) instrument of the NASA/ESA Solar and Heliospheric Observatory (SOHO) research satellite. The M_{10} index is from medium-UV flux near 280 nm measured with operational NOAA satellites. The Y_{10} index is derived from a mixture of both solar X-ray emissions in the 0.1- to 0.8-nm range, from the GOES X-ray Spectrometer (XRS) instrument, and hydrogen Lyman- α emissions obtained from the NASA TIMED satellite.

Table 1
Comparison of Modeled and Measured Values of Exospheric Temperatures

Model version	Mean absolute deviation (° K)	Mean standard deviation (° K)
0	37.31	52.03
1	53.03	72.00
2	30.95	42.81
3	28.17	38.58
4	28.19	38.27
5	27.96	37.97
6	27.92	37.53

These indices were tested against the temperature values within each grid cell (that also contained associated dates and times for each measurement) to see how well they could fit these data. It was found that the S_{10} and M_{10} indices both had the highest correlations (using the maximum correlation in all 1,620 cells), both around 0.97, while the correlations of F_{10} and Y_{10} were about 0.95 and 0.96, respectively. As the indices are correlated with each other, a nonlinear combination is used. Trying out various powers of these indices, using a square root of the M_{10} produced a better fit. The best correlations were actually found without using any time lags or moving averages, such as the 81-day running mean (Picone et al., 2002).

The baseline model ended up using only the indices S_{10} and M_{10} , with the square root of the later. Within each cell the temperature values were fit with the equation:

$$T_{\infty} = C_0 + C_1 S_{10} + C_2 \sqrt{M_{10}} + C_3 S_{10} \sin(\theta_D) + C_4 S_{10} \cos(\theta_D) + C_5 \sqrt{M_{10}} \sin(\theta_D) + C_6 \sqrt{M_{10}} \cos(\theta_D) + C_7 \sin(2\theta_D) + C_8 \cos(2\theta_D) + C_9 \sin(\phi_{UT}) + C_{10} \cos(\phi_{UT}), \quad (1)$$

where T_{∞} is the exospheric temperature, $\theta_D = 2\pi DOY/365.25$ is the day-of-year date converted to radians, and $\phi_{UT} = 2\pi UT/24$ is the Universal Time (UT) in radians. The C_9 and C_{10} coefficients with the UT angles are for modeling the variability due to the rotation of the geomagnetic poles (which are offset from the rotational pole) through different local solar times, while the C_7 and C_8 terms are intended to capture whatever semiannual/interannual variations that are present. Since the Universal Time should not have much influence near the equator, the fit results are expected to have small values of C_9 and C_{10} in these cells while the same terms may be important elsewhere on the globe.

Initially, it had been assumed that terms for the latitude of the Sun would be required, but in actuality the day-of-year terms were sufficient for modeling the response in each cell due to the changes in the Sun's position during the year (examples will be shown in section 6). Results, summarized in Table 1, show that the mean absolute deviation for Version 0 is 37.31° K and the mean standard deviation is 52.03° K.

The ability of equation (1) to reproduce much of the exosphere's temperature variation is illustrated in Figure 2. This figure is obtained by running the EXEMPLAR model with the measured solar indices for every day of 2003, at noon on each day. The global maximum and minimum values are shown with the red and blue lines, respectively, while the global mean value of all grid cells is drawn with a green line. (This figure is actually derived from the fifth version, but uses the same coefficients in (1), as explained in section 5.6.)

4.2. Version 1: Using Only Nitric Oxide Emissions

The next version uses only the SABER measurements of the nitric oxide emissions, in order to determine whether or not these can be used as an indicator of exospheric temperatures. Why this hypothesis would be considered is shown with the graph in Figure 3. The points plotted in this figure were obtained by simply selecting all values of the NO emissions that were within a particular range and then calculating the mean value of the associated temperatures. This is done for each grid cell, and then the largest and smallest values on the sphere are found. The red and blue lines show these global, maximum, and minimum values, after repeating for different NO emissions. The green line shows the mean values. A similar result was previously shown in Figure 8 by Weimer et al. (2016).

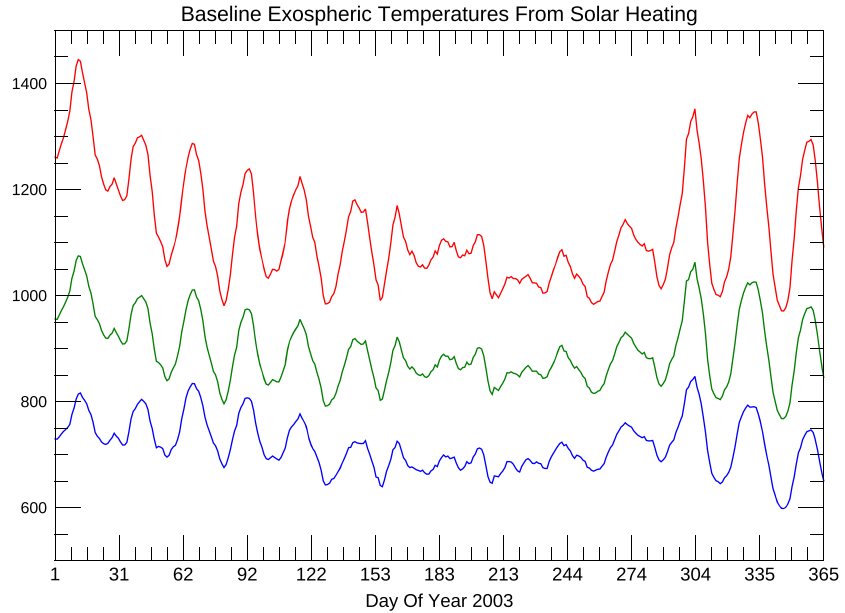


Figure 2. Exospheric temperature variations reproduced from solar indices alone. Model temperatures were calculated for every day of the year 2003, with global maximum and minimum values shown with the red and blue lines. Green line shows of the global mean value, calculated from all 1,620 grid cells.

While the NO emissions are expected to be an exponential function of the thermospheric temperatures (Mlynczak et al., 2005), in the formulas that follow, we require a way to estimate the temperatures from the global emissions. The black line in Figure 3 shows the square root of the nitric oxide emission values, scaled to match the green line, showing that the mean exospheric temperatures are approximately proportional to this square root. With this relationship, Version 1 of the EXEMPLAR model used this equation:

$$\begin{aligned}
 T_{\infty} = & C_0 + C_1 \sqrt{NO} + C_2 \sqrt{NO} \sin(\theta_D) + C_3 \sqrt{NO} \cos(\theta_D) + \\
 & C_4 \sin(2\theta_D) + C_5 \cos(2\theta_D) + \\
 & C_6 \sin(\phi_{UT}) + C_7 \cos(\phi_{UT}) + \\
 & C_8 \sqrt{NO} \sin(\phi_{UT}) + C_9 \sqrt{NO} \cos(\phi_{UT}),
 \end{aligned} \tag{2}$$

where NO represents the total power of the nitric oxide emissions measured by the SABER instrument. There are two sets of coefficients that model the response as a function of UT. Coefficients C_6 and C_7 are for reproducing the variations with low levels of geomagnetic activity, while C_8 and C_9 are intended to reproduce auroral oval variations during more active times, when the nitric oxide emissions are generally larger. This version produced a mean absolute deviation of 53.03° K and a mean standard deviation of 72.00° K . While this is not a terrible result, these deviations are still significantly worse than obtained with only the solar indices. This result is not totally unexpected, as the NO emissions originate well below the exosphere and are driven by the local composition and temperature in the lower thermosphere (120–150 km). As the nitric oxide power is highly correlated with the auroral heating that occurs at high latitudes (Weimer et al., 2015), it appears that the solar indices need to be included in order to model conditions at both high and low latitudes.

4.3. Version 2: Combining Nitric Oxide Emissions With Solar Indices

The next trial combined together the previous two versions, with the assumption that the nitric oxide emissions would follow the temperature changes due to geomagnetic activity/auroral heating that the solar indices could not:

$$\begin{aligned}
 T_{\infty} = & C_0 + C_1 \sqrt{NO} + C_2 S_{10} + C_3 \sqrt{M_{10}} + \\
 & C_4 \sqrt{NO} \sin(\theta_D) + C_5 \sqrt{NO} \cos(\theta_D) + C_6 S_{10} \sin(\theta_D) + C_7 S_{10} \cos(\theta_D) + \\
 & C_8 \sqrt{M_{10}} \sin(\theta_D) + C_9 \sqrt{M_{10}} \cos(\theta_D) + C_{10} \sin(2\theta_D) + C_{11} \cos(2\theta_D) + \\
 & C_{12} \sin(\phi_{UT}) + C_{13} \cos(\phi_{UT}) + C_{14} \sqrt{NO} \sin(\phi_{UT}) + C_{15} \sqrt{NO} \cos(\phi_{UT}).
 \end{aligned} \tag{3}$$

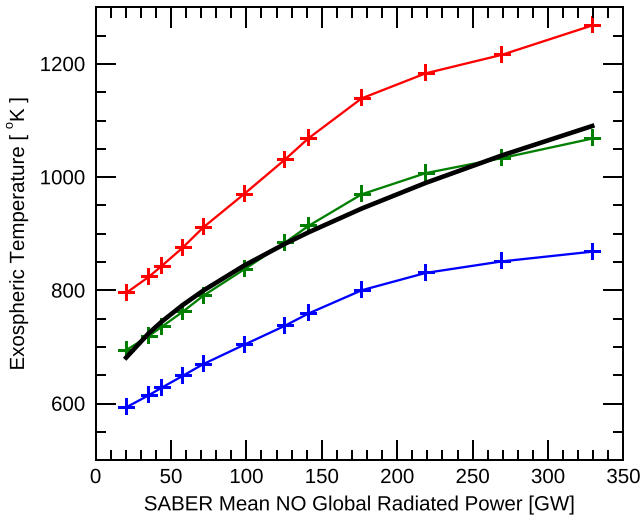


Figure 3. Exospheric temperature as a function of nitric oxide emission power. The red line shows the maximum exospheric temperature on a global map, and the blue line shows the minimum value, compared with the simultaneously measured total radiated power from nitric oxide. The green line shows the global, mean temperature, while the black line shows the square root of the radiated power, scaled to match.

This formula produced a mean absolute deviation of 30.95° K and a mean standard deviation of 42.81° K. Therefore, this combined version did perform better than either of the two versions alone. The importance of the terms containing the Universal Time will be demonstrated in section 6.

4.4. Version 3: Adding Polar Heating Calculated From a Poynting Flux Model

While the addition of the nitric oxide emissions to the version that uses solar indices does produce better fits with the data, these emissions are related to the auroral heating energy that has been already added to the system during the previous hours or days, and offset by the amount of radiative cooling present. Near the geomagnetic poles it is possible that the exospheric temperatures and neutral density may respond to more short-term auroral heating. In order to investigate this possibility, we calculate the total Poynting flux into the polar regions using the electrodynamic models described by Weimer (2005a, 2005b), also referred to as the W05 model. The electric field model is used in combination with the field-aligned current model, which provides the magnetic perturbation vector, to calculate the total flux into both the Northern and Southern Hemispheres. The required model inputs were obtained from measurements of the Interplanetary Magnetic Field (IMF) and solar wind velocity on the Advanced Composition Explorer (ACE) spacecraft.

The equation used in this version is

$$T_{\infty} = C_0 + C_1 \sqrt{NO} + C_2 S_{10} + C_3 \sqrt{M_{10}} + C_4 \sqrt{NO} \sin(\theta_D) + C_5 \sqrt{NO} \cos(\theta_D) + C_6 S_{10} \sin(\theta_D) + C_7 S_{10} \cos(\theta_D) + C_8 \sqrt{M_{10}} \sin(\theta_D) + C_9 \sqrt{M_{10}} \cos(\theta_D) + C_{10} \sin(2\theta_D) + C_{11} \cos(2\theta_D) + C_{12} \sin(\phi_{UT}) + C_{13} \cos(\phi_{UT}) + C_{14} S_T \sin(\phi_{UT}) + C_{15} S_T \cos(\phi_{UT}) + C_{16} S_T \quad (4)$$

where S_T represents the Poynting flux totals, which replaced the nitric oxide in the C_{14} and C_{15} terms associated with the UT variations, as well as one additional term applied without modification, in C_{16} . The least error fit using equation (4) is applied uniformly to every grid cell. On the other hand, we have Poynting flux totals that are calculated separately for the Northern and Southern Hemispheres, and the temperatures in the grid cells near each pole should be matched with the amount of heating in that same pole, while the cells at low latitudes respond to both. Therefore, these hemispheric totals are combined together using

$$S_T = S_N \sin^2(0.5 * (Latitude + \pi/2)) + S_S \sin^2(0.5 * (Latitude - \pi/2)), \quad (5)$$

where S_N and S_S are the Poynting flux totals in each hemisphere and the latitude is that of each grid cell's geometric center, in radians, in the range of $-\pi/2$ to $+\pi/2$. This equation produces a smooth transition of the Poynting flux totals from one hemisphere to the other.

The Poynting flux totals are actually evaluated as an average over some period of time. Through trials of various time intervals it was found that the errors were lowest if the auroral heating was averaged over the previous 13 hr. This version resulted in a mean absolute deviation of 28.17° K and a mean standard deviation of 38.58° K, which are better than the prior versions.

4.5. Version 4: Rising and Falling Temperature Perturbations

It is known that the temperature of the thermosphere rises during times of high geomagnetic activity and, after the enhanced heating stops, decays at an exponential rate (Burke et al., 2009; Wilson et al., 2006). It is also known that the enhancement to the nitric oxide that occurs during geomagnetic storms can accelerate the cooling (Lei et al., 2012; Mlynczak et al., 2003). This behavior in the temperature is explicitly built into the JB2008 model [Bowman et al., 2008], which uses an input parameter, ΔT_c , that accounts for this behavior of the exospheric temperature. This ΔT_c is derived from the Dst index (Burke et al., 2009) if Dst is under -75 nT; otherwise, the 3-hr ap indices are used. The ΔT_c value is updated hourly. The MSIS model also includes temperature perturbations that are calculated from the daily Ap and hourly ap indices.

Weimer et al. (2011) had developed an improvement to the ΔT_c parameter for the JB2008 model, using the W05 model to calculate the rise of the temperature correction at each time step, and the amount of heat energy also increased another variable in the equations that caused the temperature to decay at a faster rate. In the evaluations done by the NASA Community Coordinated Modeling Center (CCMC) (Shim et al., 2012), it was found that both the original and modified JB2008 model had the best root-mean-square error and prediction efficiency, in comparison to four other models, while the MSIS model always did better on the ratio of the maximum change in density. Later, Weimer et al. (2015) had improved on the temperature calculations, while showing how well the NO emissions measured with the SABER instrument correlated with the heating rates.

Since the two versions of the JB2008 model did better than the MSIS model in the evaluations by the CCMC, it is reasonable to assume that use of these temperature perturbations may be more accurate than what the MSIS model derives from the geomagnetic activity indices. On the other hand, we note that the tables shown by Bruinsma et al. (2018) give the impression that MSIS performed better than the standard JB2008 model, while the Drag Temperature Model 2013 (DTM2013) (Bruinsma, 2015) generally did better than both. Several different metrics were used.

The JB2008 model uses very low order/degree spherical harmonics to evaluate the global exospheric temperatures, so it does not have high spatial resolution, particularly at high latitudes. The ratio between the maximum and minimum exospheric temperature is also fixed in this model, while Figure 3 shows that this ratio increases as the temperature increases. These are two reasons why the MSIS model was able to do better on other metrics. It is reasonable to assume that a greater spatial resolution would help.

So the fourth version of the EXTEMLAR model tries the same strategy as JB2008, but at much better resolution. A temperature correction factor replaces the NO emission terms, as well as the polar heating terms:

$$T_{\infty} = C_0 + C_1 \Delta T + C_2 S_{10} + C_3 \sqrt{M_{10}} + C_4 \Delta T \sin(\theta_D) + C_5 \Delta T \cos(\theta_D) + C_6 S_{10} \sin(\theta_D) + C_7 S_{10} \cos(\theta_D) + C_8 \sqrt{M_{10}} \sin(\theta_D) + C_9 \sqrt{M_{10}} \cos(\theta_D) + C_{10} \sin(2\theta_D) + C_{11} \cos(2\theta_D) + C_{12} \sin(\phi_{UT}) + C_{13} \cos(\phi_{UT}) + C_{14} \Delta T \sin(\phi_{UT}) + C_{15} \Delta T \cos(\phi_{UT}) \quad (6)$$

where ΔT is the temperature correction. This correction ΔT at each point in time is calculated from

$$\Delta T(t_{n+1}) = \Delta T(t_n) - \Delta T(t_n) \left(\frac{\delta t}{\tau_c} \right) + \alpha S_T(t_n) - \beta R_{NO_M}(t_n), \quad (7)$$

where δt is the numerical time step (4 min), τ_c is the exponential cooling rate, and α is a factor that scales the temperature increase in each time step relative to the Poynting flux (S_T). The measured values of the total power radiated from nitric oxide (R_{NO_M} ; from the SABER instrument) are used to decrease the temperature in each time step, in proportion to the scaling factor β . The parameters (α , β , and τ_c) were empirically determined through reiterative adjustments that minimized the error in (6), in comparison with all of the derived temperatures, with the result that $\alpha = 0.00771^\circ \text{ K/GW}$, $\beta = 0.0001965^\circ \text{ K/GW}$, and $\tau_c = 9.671 \text{ hr}$. An additional saturation parameter was also determined for the total heating from the W05 model, rolling over at 763 GW. While the total nitric oxide power used was from daily totals, these numbers were interpolated to the same, 4-min time intervals in which the W05 heating was calculated.

This version resulted in a mean absolute deviation of 28.19° K and a mean standard deviation of 38.27° K . While the standard deviation was better, the former was worse than the previous version, but just by a very small margin.

4.6. Version 5: Short-Term Auroral Heating Reintroduced

The calculation of the temperature correction in equation (7) basically integrates the level of auroral heating from past time intervals, which should be appropriate for low latitude regions. However, near the poles the more recent heating should be more relevant, which is the explanation for why (6) was not that much better than (4). So the next trial reintroduced the Poynting flux in the UT terms (which mainly define the location

of the geomagnetic poles and auroral ovals), which retains the ΔT values that have a more global influence:

$$\begin{aligned}
 T_{\infty} = & C_0 + C_1 \Delta T + C_2 S_{10} + C_3 \sqrt{M_{10}} + \\
 & C_4 \Delta T \sin(\theta_D) + C_5 \Delta T \cos(\theta_D) + C_6 S_{10} \sin(\theta_D) + C_7 S_{10} \cos(\theta_D) + \\
 & C_8 \sqrt{M_{10}} \sin(\theta_D) + C_9 \sqrt{M_{10}} \cos(\theta_D) + C_{10} \sin(2\theta_D) + C_{11} \cos(2\theta_D) + \\
 & C_{12} \sin(\phi_{UT}) + C_{13} \cos(\phi_{UT}) + C_{14} S_T \sin(\phi_{UT}) + C_{15} S_T \cos(\phi_{UT}) + C_{16} S_T
 \end{aligned} \quad (8)$$

Everything is the same as in (6) and (7), except that it was found that the averaging period used to calculate S_T could be reduced from 13 down to 2 hr to get the lowest errors, as the longer-term effects of the heating at lower latitudes are already included in ΔT . The result was a mean absolute deviation of 27.96° K and a mean standard deviation of 37.97° K, which is an improvement over Version 4.

All of the terms in (8) that are not present in (1) account for the additional heating of the thermosphere due to auroral activity. If these additional terms are not used to calculate the exospheric temperatures, then the results show the influence of only the solar radiation and the annual and semiannual terms, as the geomagnetic activity adds to the solar response that was fit with (1). So while equation (1) was used to obtain the graphs shown in Figure 2, the results from this version were actually used for this graph, and the terms in (8) that do not appear in (1) were not used.

4.7. Version 6: Using a Numerical Version of Nitric Oxide Cooling

The previous results show that satellite measurements of nitric oxide emissions indeed can be used to improve the predictions of exospheric temperatures, either directly as in Versions 2 or 3 or through a calculation of temperatures in a difference equations, as in Versions 4 and 5. However, at present such measurements are not readily available in the time frame needed for actual predictions in real time. Therefore, this final version replaces the measured nitric oxide cooling in (7) with one derived from numerical, difference equations:

$$\Delta T(t_{n+1}) = \Delta T(t_n) - \Delta T(t_n) \left(\frac{\delta t}{\tau_c} \right) + \alpha S_T(t_n) - P_{NO}(t_n), \quad (9)$$

$$P_{NO}(t_n) = \beta \Delta NO(t_n) \exp \left(\frac{-2700}{\Delta T(t_n) + T_{Solar}(t_n)} \right), \quad (10)$$

$$\Delta NO(t_{n+1}) = \Delta NO(t_n) - \Delta NO(t_n) \left(\frac{\delta t}{\tau_{NO}} \right) + \gamma S_T(t_n). \quad (11)$$

P_{NO} represents the additional cooling power of the nitric oxide emissions. β is an empirical scaling factor, and $\Delta NO(t_n)$ is the simulated enhancement to the NO present at time step n . This product is multiplied by e raised to the power of $-2,700$ over the total temperature, which is the sum of the auroral $\Delta T(t_n)$ from (9) and the background solar temperature from (1). The 2,700 comes from the energy of nitric oxide 5.3 μm emissions converted to degrees Kelvin. The quantity ΔNO increases in each time step in proportion to the amount of Poynting flux, S_T , and decays exponentially with time constant τ_{NO} . These formulas are similar to those used by Weimer et al. (2015), but with a modification in (10). These simulated NO emissions were found to have a high correlation with the measured values.

As before, the free parameters in (9)–(11) were empirically determined by minimizing the error in (8). With $\Delta NO(t_n)$ increasing in proportion to the Poynting flux with the arbitrary scaling factor γ fixed at 0.0001 /GW, the result of the fit for the other parameters was $\alpha = 0.005001^\circ \text{ K/GW}$, $\beta = 0.8499^\circ \text{ K}$, $\tau_c = 9.999 \text{ hr}$, and $\tau_{NO} = 17.00 \text{ hr}$. The saturation parameter applied to the W05 model was increased to 3,100 GW for optimal results. The ΔT values calculated in this way were used in (8) for Version 6 of EXEMPLAR, resulting a mean absolute deviation of 27.92° K and a mean standard deviation of 37.53° K, a small improvement over the previous version, but still having the smallest errors of all.

5. Example Results

After the derivation of the model coefficients through the least error fits, global maps of the exospheric temperatures are obtained by simply substituting the actual or hypothetical values of the input parameters

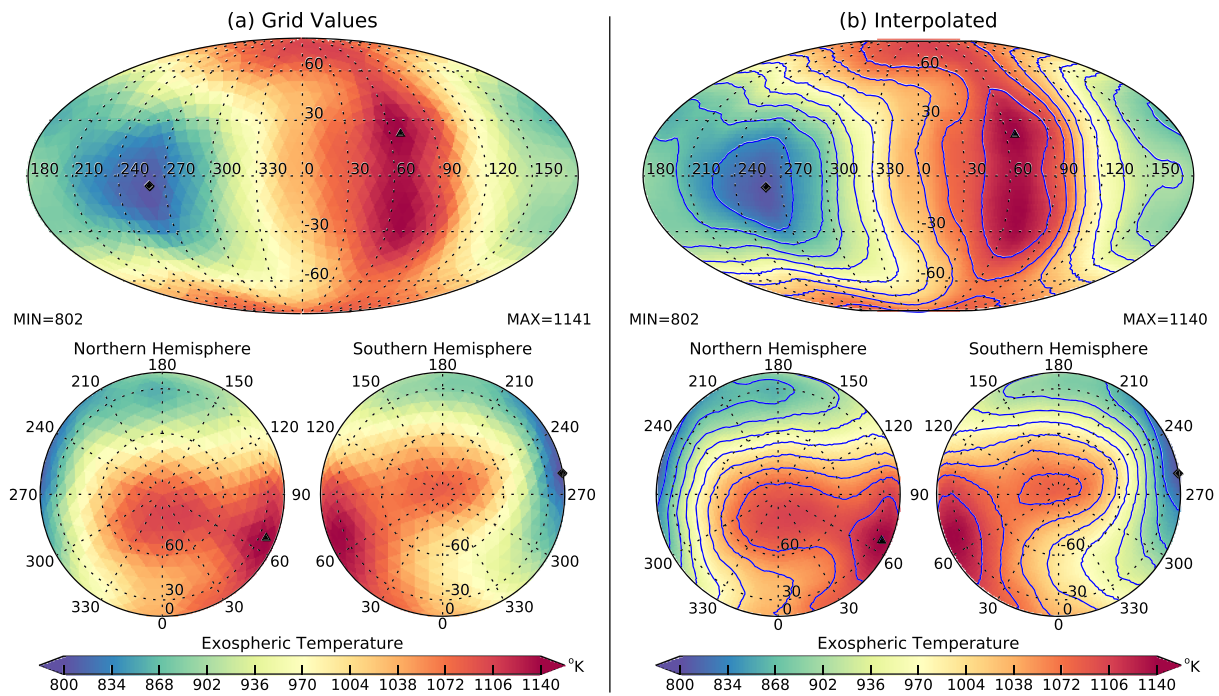


Figure 4. Example map of exospheric temperature variations calculated with the EXEMPLAR model. $\Delta T = 100^\circ \text{K}$, day of year = 80, UT = 15 hr, both S_{10} and $M_{10} = 120 \text{ sfu}$, and the polar heating is 50 GW in both hemispheres. (a) The values in each grid cell; (b) the results using a triangulated interpolation.

into the model equations for each of the 1,620 grid cells. An example of results from (8) is shown in Figure 4, with $\Delta T = 100^\circ \text{K}$, day of year = 80 (spring equinox), UT = 15 hr, both S_{10} and $M_{10} = 120 \text{ sfu}$, and the polar heating is 50 GW in both hemispheres. In Figure 4a a map is shown with each grid cell colored uniformly according to its temperature. An interpolation scheme is required in order to obtain values at a specific latitude and longitude. To accomplish this interpolation, the coordinates of the two-dimensional “center of mass” of each grid cell are determined, with the temperature in each cell assigned to these centers. These points form another set of triangles that are used in a triangular interpolation. Figure 4b shows the results of such interpolation on a higher-resolution latitude-longitude grid. Contour levels are drawn with the blue lines. Local noon solar time is at 0 longitude in this and subsequent figures.

Figure 5 shows the effects of the Universal Time variations, with parts (a)–(d) showing results for 3, 9, 15, and 21 UT. All other input conditions are the same as in the previous example, except that the polar energy flux level has been increased to 200 GW in each hemisphere, which boots the effects at high latitudes. Through evaluations at 1-hr increment, it has been found that the maximum temperature is generally found in the Southern Hemisphere around 9 UT, and in the Northern Hemisphere at 21 UT, while the two poles are roughly equal at 3 and 15 UT. The temperatures in the Southern Hemisphere tend to peak at greater levels than in the north and often seem to occupy a greater area. In comparing Figure 5c with 4b, in which everything is the same except the higher level of polar energy flux, the temperatures near both poles become greater than at the noon-time equator, while the minimum temperature, at $240\text{--}270^\circ$ longitude (4 to 6 hr local time), has actually decreased.

Figure 6 shows the effects of the day of year, with parts (a)–(d) showing results for days, 80 (21 March), 172 (21 June), 264 (21 September), and 355 (21 December). The solar indices are the same as in the other examples, the UT is 3 hr, and both ΔT and the polar energy flux are set to zero in order to isolate just the annual and semiannual variations. The spring (Figure 6a) and fall (Figure 6c) equinoxes have roughly equal temperatures, with the peak near the equator around 60° longitude (16 hr local solar time), with the spring equinox tending to be slightly warmer. Not surprisingly, at the solstices the peak temperatures move with the sun to the Northern (Figure 6b) or Southern (Figure 6d) Hemisphere. The Southern Hemisphere peak in December is 100° larger than the maximum temperature in June.

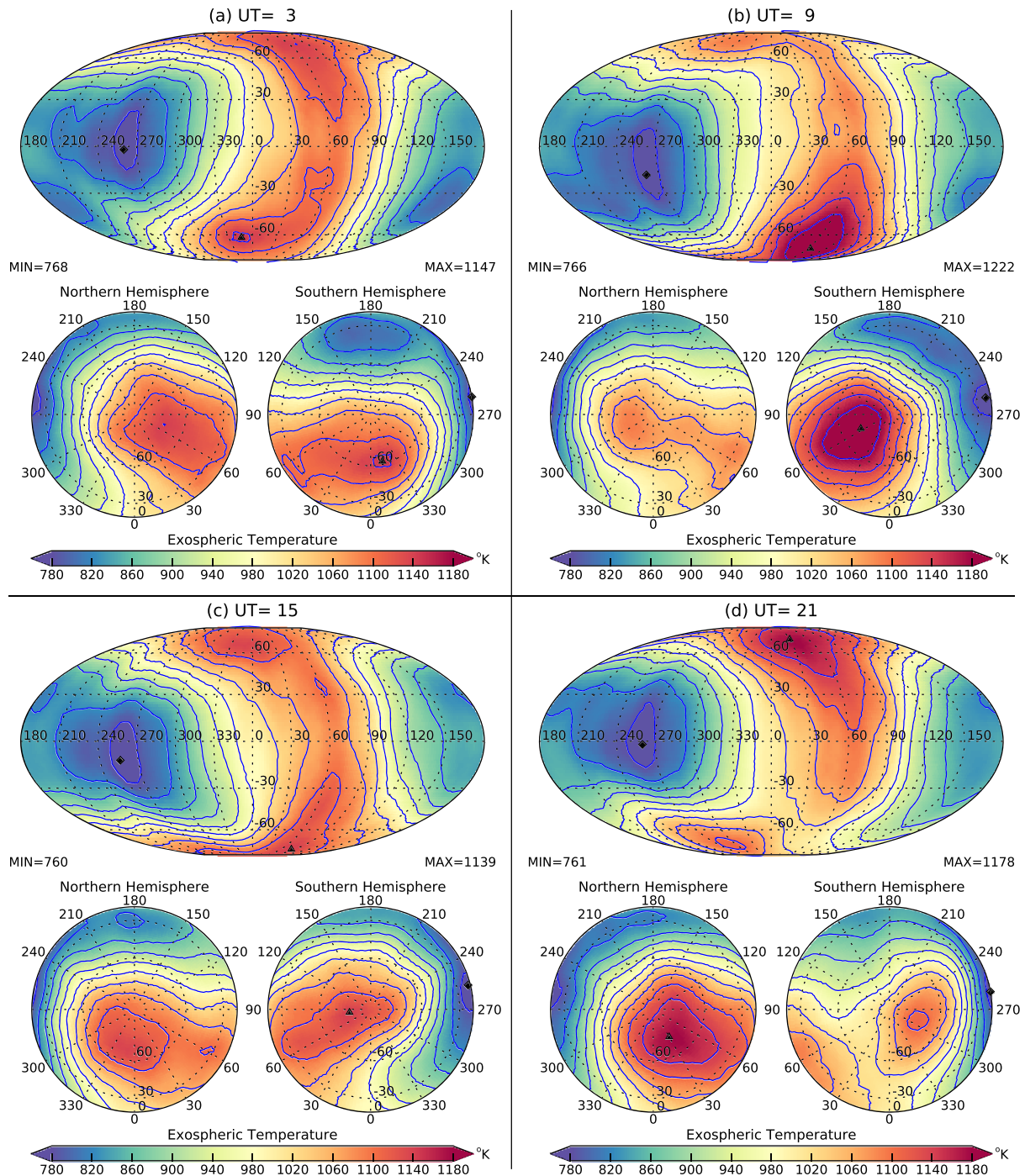


Figure 5. Examples showing how changing the Universal Time influences the maps of exospheric temperature. In a–d the UT is set to 3, 9, 15, and 21 hr, while the other parameters are fixed: $\Delta T = 100^\circ \text{K}$, day of year = 80, both S_{10} and $M_{10} = 120 \text{ sfu}$, and the polar energy flux is 200 GW in both hemispheres.

6. Predictions for Specific Time Intervals

While these examples are useful and interesting, the real test of the EXTEMLAR code is seeing how well it does in actual events. One example is taken from 26–28 July 2004, in which there was a high level of auroral activity, that followed episodes of heating on the two previous days. Figures 7 and 8 show temperature values along the orbits of the GRACE A and CHAMP satellites. The blue lines show the exospheric temperatures that were derived from the neutral densities (the “measured” values), and the red lines show the exospheric temperatures from the EXTEMLAR model. The model values on the grid have been interpolated to the

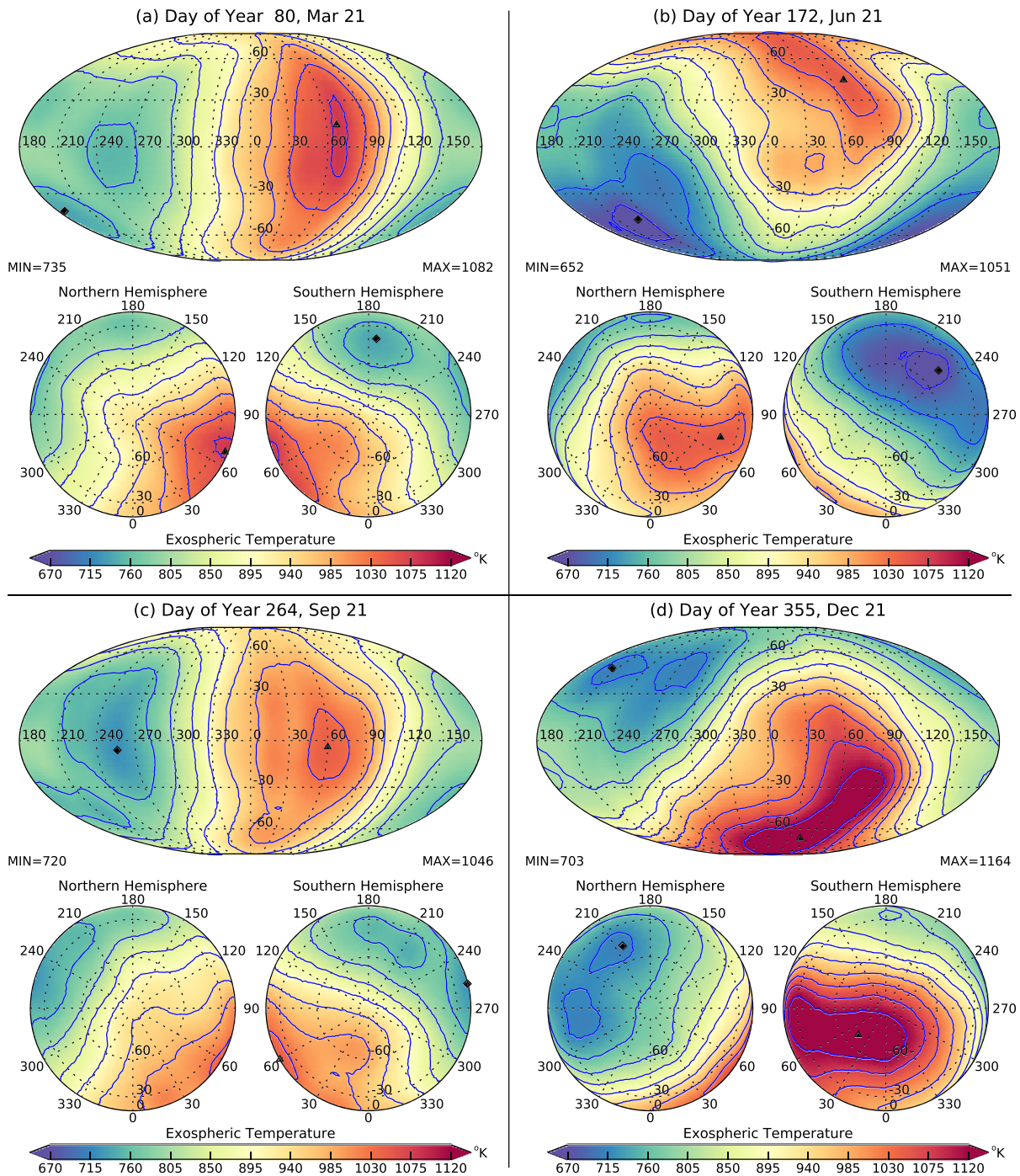


Figure 6. Examples showing how the day of year influences the maps of exospheric temperature. In a–d the day of year is set to 80, 172, 264, and 355, while the other parameters are fixed: ΔT and the polar energy flux are set to zero, UT = 3 hr, while both S_{10} and $M_{10} = 120$ sfu.

satellite's coordinates in geographic latitude and local time. The green lines show the exospheric temperatures that the MSIS model would use. These values may be elevated at the start of these graphs due to the auroral activity that occurred on the previous day. Even so, most of the time the MSIS values are actually quite close to the measured values.

The dashed, red lines in Figures 7 and 8 show the largest and smallest temperatures that are found on the global-scale grid at each time step. Interestingly, the minimum temperature value appears to decrease during the very strong heating events, while the maximum temperature increases. This behavior during

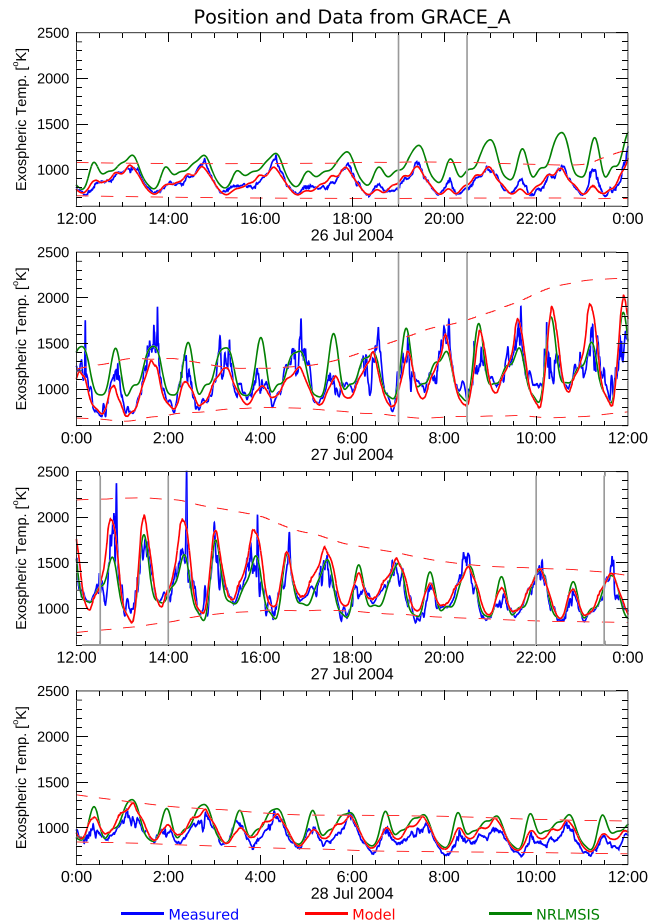


Figure 7. Example of exospheric temperatures along the GRACE A orbit, from 12 UT on 26 July to 12 UT on 28 July 2004. Solid red lines show the temperatures from the EXTEMLAR model evaluated along the orbit, while the dashed red lines show the smallest and largest values on the global grid at the same times. Blue lines show the measured values, and green lines show the temperatures in the MSIS model.

extreme geomagnetic storms will need to be investigated in future model revisions. It may perhaps be an artifact resulting from using the same delay times in the $C_1 \Delta T$ and $C_{16} S_T$ terms across the globe, while the low-latitude heating response could be delayed. The C_{16} coefficient in the Versions 5 and 6 fits is negative at low latitudes, which results in a delay in the response at low latitudes until after the polar heating turns off and, in extreme events, may overcompensate.

The four pairs of light gray vertical lines in these figures designate time intervals that are selected for use in Figure 9, which shows maps of the temperatures and both satellite orbits for these four intervals. The specific conditions used in the EXTEMLAR model are taken from the midpoint in these time intervals and are indicated in the legends at the top of each map. The orbits are overlaid with the heavy blue (GRACE A) and magenta (CHAMP) lines, starting at the round symbols and ending at the squares. Although the range of temperatures represented by the coloring was kept constant within the previous figures, in Figures 9a–9d the color bars changed in order to show the most dynamic range in each part. Figures 9b and 9c indicate that sometimes the equatorial regions are much cooler than the polar regions, where the temperature changes are the greatest. As the auroral heating levels are quite extreme in this event (over 1,000 GW at times), the effects of the statistical fluctuations mentioned earlier start to appear, manifested as either enhancements or depressions along meridional lines.

The EXTEMLAR model predictions have been compared with both the derived temperatures and the MSIS results for every day in the database, with mean errors and standard deviations computed on a day-by-day basis. These prediction errors were calculated for each day in 2002 to 2010 for which there were measurements available. The result was that on 82% of the days the EXTEMLAR model had lower errors than the

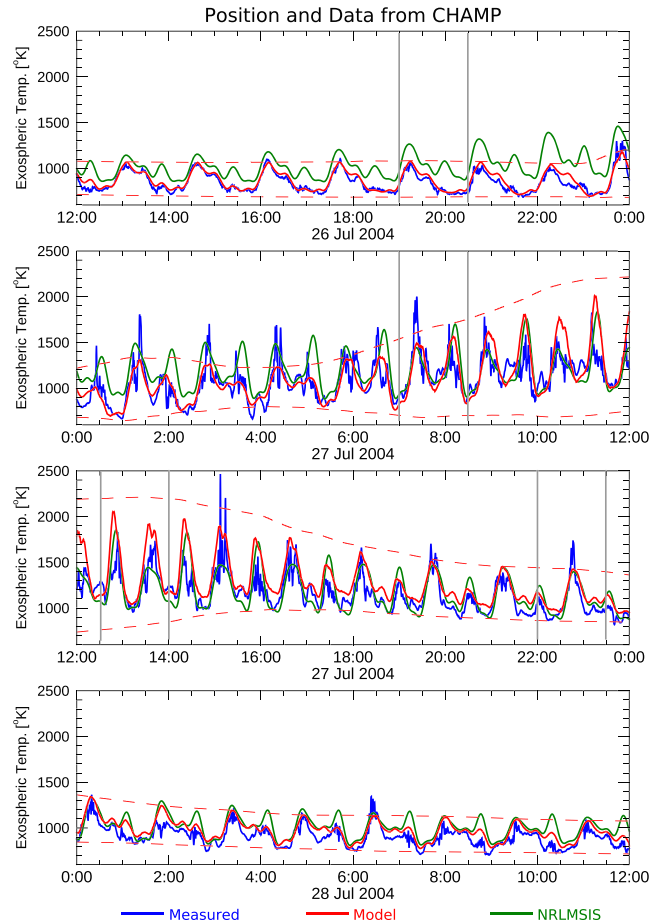


Figure 8. Example of exospheric temperatures along the CHAMP orbit, from 12 UT on 26 July to 12 UT on 28 July 2004. Solid red lines show the temperatures from the EXTEMLAR model evaluated along the orbit, while the dashed red lines show the smallest and largest values on the global grid at the same times. Blue lines show the measured values, and green lines show the temperatures in the MSIS model.

MSIS model with the CHAMP data, and it was better with the GRACE A measurements on 84% of the days. In 2014 to 2017 the new model does better than MSIS 80% of the time for the Swarm A measurements, and 75% for Swarm B. To be fair, we note that none of these data were available to the developers at the time that the 2000 version of the MSIS model was constructed. The Swarm B measurements from 2017 were not used in the development of EXTEMLAR, and in trying the same tests for that year, the same level of improvement was found, although geomagnetic activity in 2017 was low.

7. Comparisons With Neutral Density Measurements

A more important test is to determine how well the EXTEMLAR model does at predicting the neutral densities. The MSIS code is required in order to do so, substituting for the exospheric temperature values that MSIS would use. As the database was constructed using all MSIS options turned on, it needs to be used in the same way, including the measured values of the solar $F_{10.7}$ index and geomagnetic activity indices. These parameters influence the conditions at the 120-km altitude boundary that MSIS uses to calculate the density altitude profiles, given the exospheric temperature. Conditions at this boundary are not the same across the globe, so as a result the global maps of the neutral densities do not necessarily vary in lockstep with the exospheric temperatures.

Returning to the same time period that was shown previously, Figures 10 and 11 show the neutral densities on 26–28 July 2004. The solid red lines in the figures show the neutral density that results from using the new exospheric temperatures, substituted in the MSIS model, while the blue lines show the measured values

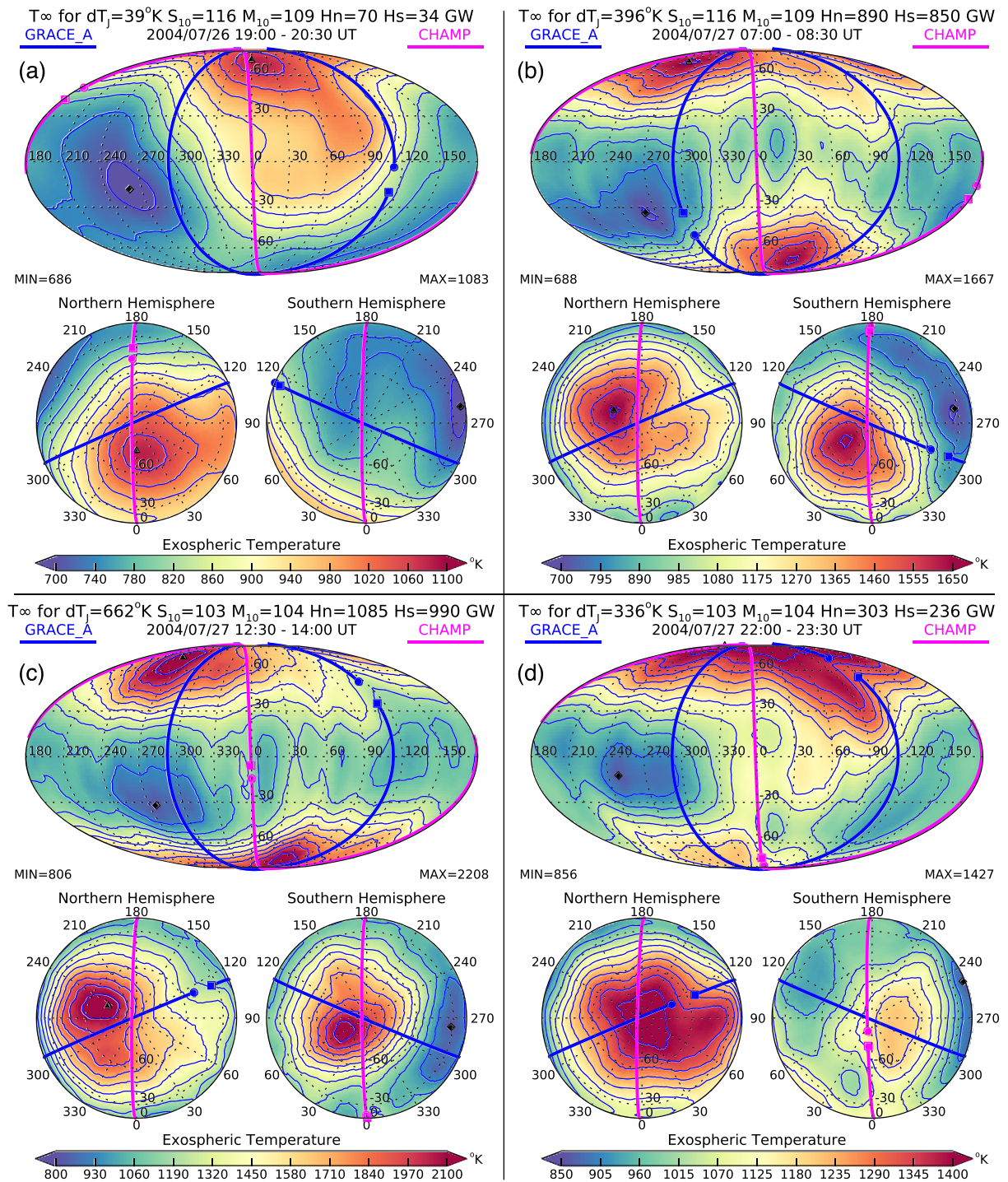


Figure 9. Global maps of exospheric temperatures at selected intervals on 26–27 July 2004. The maps are overlaid with the orbital paths of the GRACE A (blue) and CHAMP (magenta) satellites, starting and ending at the times indicated at the top, which correspond to the vertical, gray lines in Figures 7 and 8. The starting and ending points of these paths are indicated with the round and square dots. EXTEMLAR model input parameters, shown at the center of each interval, with H_n and H_s indicating the amount of heating in the Northern and Southern Hemispheres.

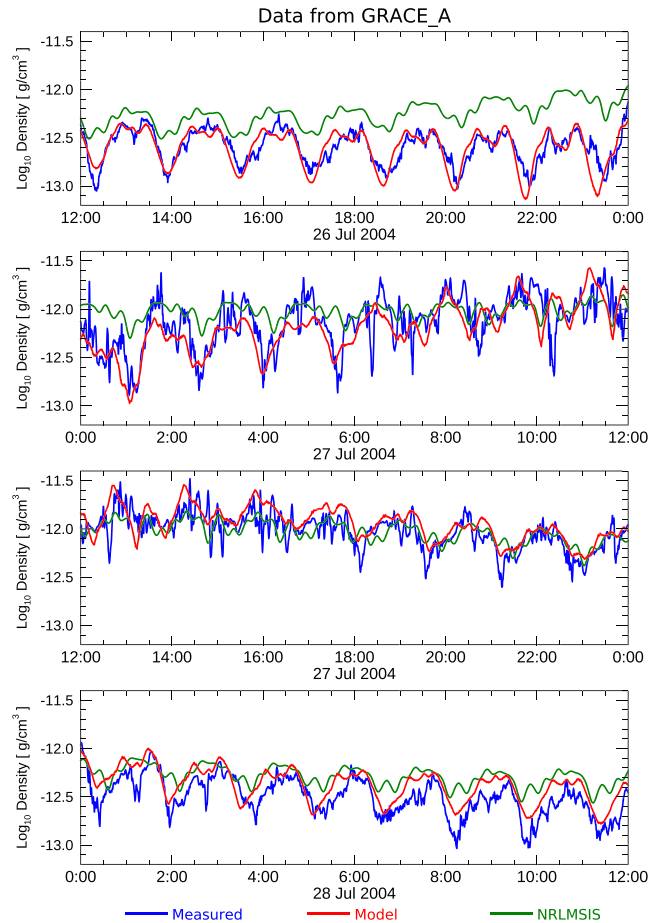


Figure 10. Example of neutral densities along the GRACE A orbit, from 12 UT on 26 July to 12 UT on 28 July 2004. Solid red lines show the density from the EXTEMLAR model evaluated along the orbit. Blue lines show the measured values, and green lines show the densities from the MSIS model.

on GRACE A (Figure 10) and CHAMP (Figure 11). The green lines show the density obtained from the unmodified MSIS model.

Comparing the errors in the model versus measured neutral densities on a day-by-day basis, the percentages are basically the same as with the temperature comparisons, with the EXTEMLAR-MSIS combination performing better than MSIS alone about 80% of the time. The density correction factors mentioned previously were applied to both model calculations equally.

While the data from the GOCE satellite was not used for building the new model, its performance relative to MSIS could be compared for the neutral density predictions using this data set. From late 2009 to 2012, EXTEMLAR performed better on average 72% of the time, although the rate drops to only 32% in 2013, when MSIS alone seems to do better while the altitude of GOCE was decreasing.

The densities computed from the EXTEMLAR-MSIS combination were also compared with results from the JB2008 model along the satellites orbits, and it did better than JB2008 on 80% of the GRACE A data. For CHAMP, the rate was 79%, and for the GOCE data it was 70% on average, as well as in 2013. For the years 2014 to 2016, the improvement was 71% for Swarm A and 47% for Swarm B. The anomalies were in 2017, when the EXTEMLAR-MSIS combination did better than JB2008 for only 50% of the Swarm A density measurements and only 2% of the time for Swarm B.

Returning to Figures 10 and 11, there are features worth noting. During the first 6 hr of 27 July, prior to the time of Figure 9b, both GRACE A and CHAMP show density values that remain persistently low at low latitudes, while the polar regions are experiencing substantial density increases. This delayed, low-latitude response has been seen in other major geomagnetic storms.

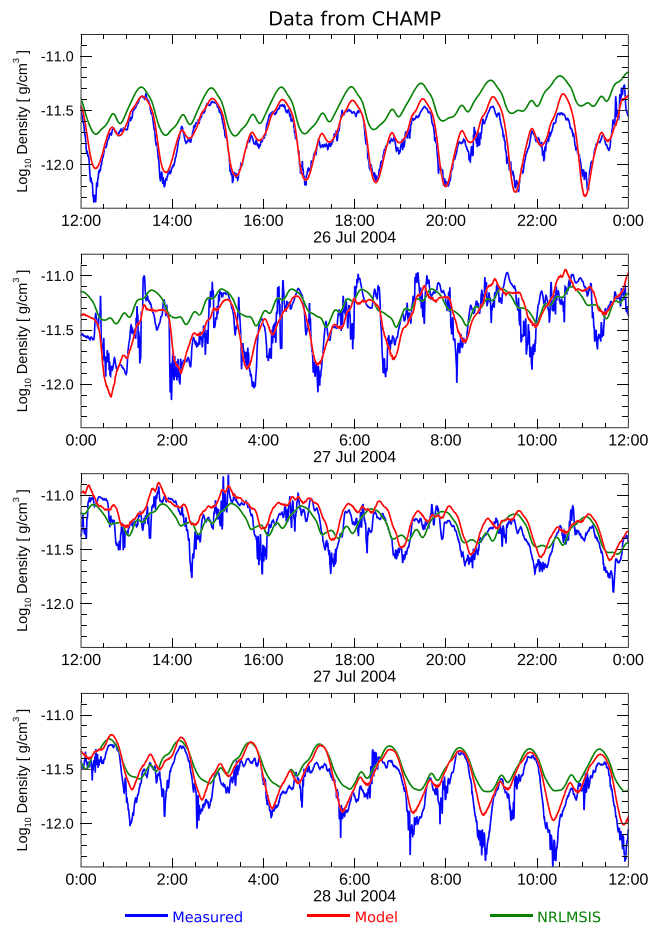


Figure 11. Example of neutral densities along the CHAMP orbit, from 12 UT on 26 July to 12 UT on 28 July 2004. Solid red lines show the density from the EXEMPLAR model evaluated along the orbit. Blue lines show the measured values, and green lines show the densities the MSIS model.

The electronic supplement contains additional graphs, similar to those shown in Figures 10 and 11, for a number of space weather events of interest. Predictions from the JB2008 model are also included on these supplemental graphs. The selected time intervals include those listed by Shim et al. (2012) for the “Coupling and Energetics of Atmospheric Regions (CEDAR) Electrodynamics Thermosphere Ionosphere (ETI) Challenge.” Four other events of interest to the CEDAR program are included, along with eight other time periods of interest. Nearly all of the events listed by Bruinsma et al. (2018) are covered.

8. Conclusion

Neutral density measurements taken on the GRACE A, CHAMP, and Swarm satellites have been used to derive the exospheric temperatures that are required in the MSIS model in order to exactly match these measurements. These temperatures have been incorporated into the new model named EXEMPLAR, which is based on least error fit solutions calculated within separate cells on a geodesic grid. Seven different solutions are presented, in order to introduce the different terms and demonstrate step-by-step how the fits are improved. Use of the energy flowing into the high-latitude regions, obtained from the W05 empirical model (Weimer, 2005a, 2005b), is required to obtain the best results.

During geomagnetic storms the largest temperature and density increases are found near the poles, where the energy dissipation from the solar wind and magnetosphere takes place. The EXEMPLAR model results show that the locations of the highest exospheric temperatures are strongly influenced by the Universal Time, although this is not exactly new since the original MSIS model also includes UT variations. It is not a surprising result, as the rotation of the magnetic poles around the geographic pole is expected to produce such variations. On the other hand, the temperature enhancements in the Southern Hemisphere are found

to be greater, and cover wider areas, than those seen in the Northern Hemisphere 12 hr later under identical conditions; these findings may be new. The Southern Hemisphere was found to have much greater temperatures at the December solstice than those found in the Northern Hemisphere at the June solstice.

Future work to compare the derived exospheric temperatures with temperatures from TIMED Global Ultraviolet Imager instrument (Meier et al., 2015) and ground-based nighttime FabryPerot interferometer red-line thermosphere measurements, for example, Harding et al. (2017), over the same time intervals would be valuable. Improvement in total mass density and exospheric temperature will also likely improve first principles calculations such as the Global Ionosphere-Thermosphere Model (GITM) [Ridley et al., 2006] and Another Model of the Ionosphere (SAMI3) (Huba et al., 2008; Huba & Krall, 2013) for space-weather applications. In the latter, daytime electron density photoproduction calculations are sensitive (i.e., correlated) to total mass density through calculation of photoproduction rates (Emmert et al., 2014).

Comparing the exospheric temperatures from the EXTEMLAR model with the original measurements demonstrates that it is capable of reproducing the derived temperature values quite well, even during events with strong levels of geomagnetic activity. Neutral densities can be calculated from the predicted exospheric temperatures; the MSIS model is required for this calculation. Comparing these neutral densities that are derived from the EXTEMLAR model with the satellite measurements shows that the MSIS model predictions can be improved upon using this technique. This combination should be very useful for predicting satellite orbits with greater accuracy, especially following geomagnetic storms. Final assessment of the performance should be done independently, such as by the CCMC. As shown in Figures 10 and 11, while this model produces better predictions of the neutral density, the results are not perfect.

The results obtained with the basis functions and methodology chosen for the EXTEMLAR model demonstrate the potential for significant improvements over existing empirical exospheric temperature and total mass density specifications. EXTEMLAR is in the initial development stages, and with further work it should be possible to make improvements. One particular method for upgrading the calculations would be the addition of time delays that could vary according to location, for quantities such as the solar indices, the ΔT temperature changes, and the level of heating in the poles.

Acknowledgments

Daniel Weimer was supported by NASA Grant NNX17AC04G to Virginia Tech, with additional support from a subcontract to Hampton University, on NASA Grant NNX15AE05G. M. G. M. acknowledges support from the NASA Heliophysics Division Thermosphere-Ionosphere-Mesosphere Energetics and Dynamics Project. D. P. D and J. T. E. acknowledge support from the Office of Naval Research. The CHAMP and GRACE neutral density data are available online (at <http://tinyurl.com/RSM-Models>). The density measurements from Swarm, the L2 DNSxPOD data product, can be obtained online (through the website https://swarm-diss.eo.esa.int/#swarm%2FLevel2daily%2FLatest_baselines%2FDNS%2FPOD). The code for the NRLMSISE-00 neutral density model is available from the NASA CCMC (at <https://ccmc.gsfc.nasa.gov/pub/modelweb/atmospheric/msis/nrlmsise00/>). The SABER measurements of global power from carbon dioxide and nitric oxide are available at the SABER website (ftp://saber.gats-inc.com/Version2_0/SABER_cooling/). Linda Hunt generated the SABER NO data and provided manuscript corrections. The solar $F_{10.7}$ and AP indices were obtained from the Celestrak website (<http://celestrak.com/SpaceData/SW-All.txt>). The level 2 ACE data can be obtained from the NASA archives (at <ftp://cdaweb.gsfc.nasa.gov/pub/data/ace>). The solar indices (found at <http://sol.spacenvironment.net/JP2008/indices>) are provided by Space Environment Technologies. A data archive containing the supplemental graphs of neutral density predictions can be accessed online (at <https://doi.org/10.5281/zenodo.3525166>). Also contained here are the adjustments to the NRLMSISE-00 model supplied by J. Emmert; the total Poynting flux into both Northern and Southern Hemispheres from the Weimer 2005 model, for years 2002–2017; the derived ΔT values; and EXTEMLAR model code with the required files.

Acronym

CCMC	Community Coordinated Modeling Center
CHAMP	Challenging Mini-satellite Payload satellite
DTM2013	Drag Temperature Model 2013
EXTEMLAR	EXospheric TEMperatures on a PoLyhedral gRid
GRACE	Gravity Recovery and Climate Experiment satellite
JB2008	Jacchia-Bowman 2008 neutral density model
MSIS	Abbreviation for NRLMSISE-00
NRLMSISE-00	Naval Research Laboratory Mass Spectrometer and Incoherent Scatter radar Extended model 2000
SABER	Sounding of the Atmosphere using Broadband Emission Radiometry instrument
TIMED	Thermosphere Ionosphere Mesosphere Energetics and Dynamics satellite

References

- Astafeyeva, E., Zakharenkova, I., Huba, J. D., Doornbos, E., & van den IJssel, J. (2017). Global ionospheric and thermospheric effects of the June 2015 geomagnetic disturbances: Multi-instrumental observations and modeling. *Journal of Geophysical Research: Space Physics*, *112*, 716–11,742. <https://doi.org/10.1002/2017JA024174>
- Bowman, B. R., Tobiska, W. K., Marcos, F. A., Huang, C. Y., Lin, C. S., & Burke, W. J. (2008). A new empirical thermospheric density model JB2008 using new solar and geomagnetic indices. In *AIAA Astrodynamic Specialist Conference 18-21 August 2008, 2008-6438*. Honolulu, Hawaii.
- Bruinsma, S. (2015). The DTM-2013 thermosphere model. *Journal of Space Weather and Space Climate*, *5*, A1, 8. <https://doi.org/10.1051/swsc/2015001>
- Bruinsma, S., Sutton, E., Solomon, S. C., Fuller-Rowell, T., & Fedrizzi, M. (2018). Space weather modeling capabilities assessment: Neutral density for orbit determination at low earth orbit. *Space Weather*, *16*(11), 1806–1816. <https://doi.org/10.1029/2018SW002027>
- Bruinsma, S., Tamagnan, D., & Biancale, R. (2004). Atmospheric densities derived from CHAMP/STAR accelerometer observations. *Planetary and Space Science*, *52*, 297.
- Burke, W. J., Lin, C. S., Hagan, M. P., Huang, C. Y., Weimer, D. R., Wise, J. O., et al. (2009). Stormtime global thermosphere: A driven-dissipative thermodynamic system. *Journal of Geophysical Research*, *114*, A06306. <https://doi.org/10.1029/2008JA013848692>

- Doornbos, E., Bruinsma, S., Fritsche, B., Koppenwallner, G., Visser, P., J. van den IJssel, & J. de Teixeira de Encarnacao (2014). GOCE+ Theme 3: Air density and wind retrieval using GOCE, final report (Technical Report No. ESA 4000102847/NL/EL). European Space Agency. Retrieved from [https://earth.esa.int/documents/10174/679909/GOCEPlus Theme 3 Final Report ATBD Validation Appendices](https://earth.esa.int/documents/10174/679909/GOCEPlus+Theme+3+Final+Report+ATBD+Validation+Appendices)
- Emmert, J. T. (2009). A long-term data set of globally averaged thermospheric total mass density. *Journal of Geophysical Research*, *114*, A06315. <https://doi.org/10.1029/2009JA014102>
- Emmert, J. T., Lean, J. L., & Picone, J. M. (2010). Record-low thermospheric density during the 2008 solar minimum. *Geophysical Research Letters*, *37*, L12102. <https://doi.org/10.1029/2010GL043671>
- Emmert, J. T., McDonald, S. E., Drob, D. P., Meier, R. R., Lean, J. L., & Picone, J. M. (2014). Attribution of interminima changes in the global thermosphere and ionosphere. *Journal of Geophysical Research: Space Physics*, *119*, 6657–6688. <https://doi.org/10.1002/2013JA019484>
- Friis-Christensen, E., Lühr, H., & Hulot, G. (2006). Swarm: A constellation to study the Earth's magnetic field. *Earth, Planets and Space*, *58*(4), 351–358. <https://doi.org/10.1186/BF03351933>
- Górski, K. M., Hivon, E., Banday, A. J., Wandelt, B. D., Hansen, F. K., Reinecke, M., & Bartelmann, M. (2005). HEALPix: A framework for high-resolution discretization and fast analysis of data distributed on the sphere. *The Astrophysical Journal*, *622*, 759–771. <https://doi.org/10.1086/427976>
- Harding, B. J., Makela, J. J., Qin, J., Fisher, D. J., Martinis, C. R., Noto, J., & Wrasse, C. M. (2017). Atmospheric scattering effects on ground-based measurements of thermospheric vertical wind, horizontal wind, and temperature. *Journal of Geophysical Research: Space Physics*, *122*, 7654–7669. <https://doi.org/10.1002/2017JA023942>
- Hedin, A. E. (1991). Extension of the MSIS thermosphere model into the middle and lower atmosphere. *Journal of Geophysical Research*, *96*, 1159.
- Huba, J., & Krall, J. (2013). Modeling the plasmasphere with SAMI3. *Geophysical Research Letters*, *40*, 6–10. <https://doi.org/10.1029/2012GL054300>
- Huba, J. D., Joyce, G., & Krall, J. (2008). Three-dimensional equatorial spread modeling. *Geophysical Research Letters*, *35*, L10102. <https://doi.org/10.1029/2008GL033509>
- Lei, J., Burns, A. G., Thayer, J. P., Wang, W., Mlynczak, M. G., Hunt, L. A., et al. (2012). Overcooling in the upper thermosphere during the recovery phase of the 2003 October storms. *Journal of Geophysical Research*, *117*, A03314. <https://doi.org/10.1029/2011JA016994>
- Mehta, P. M., Walker, A. C., Sutton, E. K., & Godinez, H. C. (2017). New density estimates derived using accelerometers on board the champ and grace satellites. *Space Weather*, *15*, 558–576. <https://doi.org/10.1002/2016SW001562>
- Meier, R. R., Picone, J. M., Drob, D., Bishop, J., Emmert, J. T., Lean, J. L., et al. (2015). Remote sensing of Earth's limb by TIMED/GUVI: Retrieval of thermospheric composition and temperature. *Earth and Space Science*, *2*, 1–37. <https://doi.org/10.1002/2014EA000035>
- Mlynczak, M., Martin-Torres, F. J., Russell, J., Beaumont, K., Jacobson, S., Kozyra, J., et al. (2003). The natural thermostat of nitric oxide emission at 5.3 mm in the thermosphere observed during the solar storms of April 2002. *Geophysical Research Letters*, *30*(21), 2100. <https://doi.org/10.1029/2003GL017693>
- Mlynczak, M. G., Hunt, L. A., Marshall, T., Martin-Torres, F. J., Mertens, C. J., Russell, J. M., et al. (2010). Observations of infrared radiative cooling in the thermosphere on daily to multiyear timescales from the TIMED/SABER instrument. *Journal of Geophysical Research*, *115*, A03309. <https://doi.org/10.1029/2009JA014713>
- Mlynczak, M. G., Martin-Torres, F. J., Crowley, G., Kratz, D. P., Funke, B., Lu, G., et al. (2005). Energy transport in the thermosphere during the solar storms of April 2002. *Journal of Geophysical Research*, *110*, A12S25. <https://doi.org/10.1029/2005JA011141>
- Picone, J., Hedin, A., Drob, D., & Aikin, A. (2002). NRLMSISE-00 empirical model of the atmosphere: Statistical comparisons and scientific issues. *Journal of Geophysical Research*, *107*(A12), 1468. <https://doi.org/10.1029/2002JA009430>
- Prölss, G. W., & Bird, M. K. (2004). *Physics of the Earth's space environment: An introduction*. Berlin Heidelberg: Springer-Verlag.
- Ridley, A. J., Deng, Y., & Toth, G. (2006). The global ionosphere-thermosphere model. *Journal of Atmospheric and Solar - Terrestrial Physics*, *68*(8), 839–864. <https://doi.org/10.1016/j.jastp.2006.01.008>
- Shim, J. S., Kuznetsova, M., Rastatter, L., Bilitza, D., Butala, M., Codrescu, M., et al. (2012). Cedar electrodynamic thermosphere ionosphere (ETI) challenge for systematic assessment of ionosphere/thermosphere models: Electron density, neutral density, NmF2, and hmF2 using space based observations. *Space Weather*, *10*(10), 10004. <https://doi.org/10.1029/2012SW000851>
- Tapley, B. D., Watkins, S. B. M., & Reigber, C. (2004). The gravity recovery and climate experiment: Mission overview and early results. *Geophysical Research Letters*, *31*, L17S05. <https://doi.org/10.1029/2004GL019929>
- Tobiska, W. K., Bouwer, S. D., & Bowman, B. R. (2008). The development of new solar indices for use in thermospheric density modeling. *Journal of Atmospheric and Solar - Terrestrial Physics*, *70*, 803.
- Weimer, D. R. (2005a). Improved ionospheric electrodynamic models and application to calculating Joule heating rates. *Journal of Geophysical Research*, *110*, A05306. <https://doi.org/10.1029/2004JA010884>
- Weimer, D. R. (2005b). Predicting surface geomagnetic variations using ionospheric electrodynamic models. *Journal of Geophysical Research*, *110*, A12307. <https://doi.org/10.1029/2005JA011270>
- Weimer, D. R., Bowman, B. R., Sutton, E. K., & Tobiska, W. K. (2011). Predicting global average thermospheric temperature changes resulting from auroral heating. *Journal of Geophysical Research*, *116*, A01312. <https://doi.org/10.1029/2010JA015685>
- Weimer, D. R., Mlynczak, M. G., Emmert, J. T., Doornbos, E., Sutton, E. K., & Hunt, L. A. (2018). Correlations between the thermosphere's semiannual density variations and infrared emissions measured with the SABER778 instrument. *Journal of Geophysical Research: Space Physics*, *123*, 8850–8864. <https://doi.org/10.1029/2018JA025668>
- Weimer, D. R., Mlynczak, M. G., Hunt, L. A., & Tobiska, W. K. (2015). High correlations between temperature and nitric oxide in the thermosphere. *Journal of Geophysical Research*, *120*, 1–12. <https://doi.org/10.1002/2015JA021461>
- Weimer, D. R., Sutton, E. K., Mlynczak, M. G., & Hunt, L. A. (2016). Intercalibration of neutral density measurements for mapping the thermosphere. *Journal of Geophysical Research*, *121*, 5975–5990. <https://doi.org/10.1002/2016JA022691>
- Wenninger, M. (2014). Spherical models. Dover Publications. Retrieved from <https://books.google.com/books?id=0cfAAwAAQBAJ>
- Wilson, G. R., Weimer, D. R., Wise, J. O., & Marcos, F. A. (2006). Response of the thermosphere to Joule heating and particle precipitation. *Journal of Geophysical Research*, *111*, A10314. <https://doi.org/10.1029/2005JA011274>